Supergranule aggregation: a Prandtl number-independent feature of constant heat flux-driven convection flows

Philipp P. Vieweg[1] †

[1]Institute of Thermodynamics and Fluid Mechanics, Technische Universität Ilmenau, Postfach 100565, D-98684 Ilmenau, Germany

(Received xx; revised xx; accepted xx)

Supergranule aggregation, i.e., the gradual aggregation of convection cells to horizontally extended networks of flow structures, is a unique feature of constant heat flux-driven turbulent convection. In the present study, we address the question if this mechanism of self-organisation of the flow is present for any fluid. Therefore, we analyse three-dimensional Rayleigh-Bénard convection at a fixed Rayleigh number $\mathrm{Ra} \approx 2.0 \times 10^5$ across 4 orders of Prandtl numbers $\mathrm{Pr} \in \left[10^{-2}, 10^{2}\right]$ by means of direct numerical simulations in horizontally extended periodic domains with aspect ratio $\Gamma = 60$. Our study confirms the omnipresence of the mechanism of supergranule aggregation for the entire range of investigated fluids. Moreover, we analyse the effect of Pr on the global heat and momentum transport, and clarify the role of a potential stable stratification in the bulk of the fluid layer. The ubiquity of the investigated mechanism of flow self-organisation underlines its relevance for pattern formation in geo- and astrophysical convection flows, the latter of which are often driven by prescribed heat fluxes.

1. Introduction

Buoyancy, i.e., the interplay of gravity with mass density inhomogeneities that are typically caused by thermal heterogeneities, is – howsoever introduced – the essential mechanism that drives heat transport in many natural flows. Examples for such natural convection processes can be found on Earth throughout its layers from mantle convection (Christensen 1995) over deep ocean convection (Maxworthy and Narimousa 1994) up to convection in its atmosphere (Atkinson and Wu Zhang 1996), eventually determining local and global aspects of weather and climate.

Natural thermal convection flows reveal often a hierarchy of different flow structures such as clusters of clouds over the warm ocean in the tropics of Earth (Mapes and Houze 1993). The solar convection zone in the outer 30% of the Sun (Schumacher and Sreenivasan 2020) is another example where such a hierarchy formation appears, and might represent one of the most prominent and thoroughly studied ones. In this case, so-called *granules* are superposed to larger flow structures termed *supergranules* – while both of them are driven by the heat flux at the solar surface (Schumacher and Sreenivasan 2020; Rincon and Rieutord 2018), they offer very different lifetimes and horizontal extensions. Unfortunately, our understanding of

† Email address for correspondence: philipp.vieweg@tu-ilmenau.de

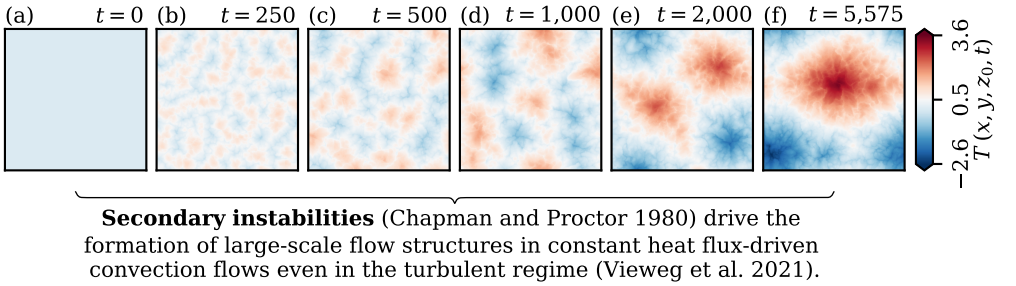

Figure 1: Gradual supergranule aggregation. While secondary instabilities are essential for the transient growth of the supergranules, the final pattern reminds of the primary instability (Hurle et al. 1967). This time series visualises a flow at $\mathrm{Pr} = 10^{-2}$ (see table 1) across the entire horizontal cross-section of aspect ratio $\Gamma = 60$ at $z_0 = 1 - \delta_T/2$ with the thermal boundary layer thickness $\delta_T = 1/(2\,\mathrm{Nu})$.

such hierarchies' origins is still far from complete (Hanson et al. 2020) and simpler setups of convection become necessary to improve it systematically.

Rayleigh-Bénard convection represents the simplest conceivable setup and thus the paradigm of naturally forced, thermally driven turbulence. Here, a fluid layer of thickness H is confined between a heated horizontal plane at the bottom and a cooled one at the top – because of the variation of density with temperature, the layer becomes unstable once subjected to gravity. As a result of intense research over the past decades, it is well-known that such convection systems organise themselves even in the fully turbulent regime into prominent *long-living large-scale flow structures*. While being clearly distinguishable from the smaller-scale turbulence or fluctuations on significantly shorter time scales, the nature of these large-scale flow structures is complex and multi-factorial.

Interestingly, only very recent research identified *thermal boundary conditions* as the key factor in determining the nature of these long-living large-scale flow structures given a horizontally extended domain. In a nutshell, either so-called *turbulent superstructures* with characteristic horizontal extensions of $\Lambda \sim O(H)$ form (Käufer et al. 2023; Stevens et al. 2018; Pandey et al. 2018; Krug et al. 2020), or a so-called *gradual supergranule aggregation* takes place that might result in a domain-sized flow structure with $\Lambda \gg O(H)$ if not interrupted by additional mechanisms such as rotation around the vertical axis (Vieweg et al. 2021, 2022). While the former establishes if the horizontal planes offer uniform temperatures (so-called Dirichlet conditions), the latter correspond to planes that prescribe a uniform vertical temperature gradient or, in other words, a spatially constant heat flux (Neumann conditions). Furthermore, the supergranules are superposed to significantly smaller (yet large-scale) granule-like flow structures, so a hierarchy of different horizontally extended flow structures may establish even in a simple turbulence configuration. This impact of thermal boundary conditions extends also to the Lagrangian material transport and the present coherent features in the flow (Vieweg et al. 2021a; Schneide et al. 2022; Vieweg et al. 2024). Remarkably, these different self-organisations of the flows persist in the numerically reachable range of large Rayleigh numbers $\mathrm{Ra} \lesssim 10^8$ (which quantify the strength of the thermal driving) (Vieweg et al. 2021, 2022). Hence, the way how buoyancy effects are prescribed at the planes or boundaries seems to eventually determine the large-scale nature of the flows in between.

Exceeding a critical value of thermal driving, the buoyancy-induced destabilisation leads to an onset of convection. While this critical value depends on the thermal boundary conditions, the latter modify in particular the horizontal extension of the emerging flow structures. In more detail, this *primary* instability leads to critical wave numbers of $k_{\mathrm{h,\,crit}} = [2.22, 3.13]$

(Rayleigh 1916; Pellew and Southwell 1940) or $k_{\mathrm{h,\,crit}} = 0$ (Hurle et al. 1967) for applied uniform temperatures or vertical temperature gradients, respectively. This latter value is further supported by the *secondary* instability, revealing that 'each mode is unstable to one of longer wavelength than itself, so that any long box will eventually contain a single roll' (Chapman and Proctor 1980). Remarkably, a leading Lyapunov vector stability analysis discovered for a Prandtl number $\mathrm{Pr} = 1$ (which defines the working fluid) that the gradual supergranule aggregation is driven by such secondary instabilities (Vieweg et al. 2021; Chapman and Proctor 1980), see also figure 1. Once the numerically finite horizontal extent of the domain is reached, the *final* statistically stationary state resembles essentially a finite size relic of critical mode and thus shares similarities with the primary instability. Crucially, the latter is independent of the working fluid, whereas secondary and subsequent instabilities depend at least in the classical case of prescribed temperatures strongly on the working fluid (Busse 1978, 2003). In the case of a prescribed heat flux, the authors studying secondary instabilities stated that their 'results hold quite generally for all Prandtl numbers' (Chapman et al. 1980) but simultaneously 'do not expect the theory to remain accurate for very small Pr' (Chapman and Proctor 1980). As the final supergranule results from the preceding transient supergranule aggregation, clarifying this uncertainty becomes crucial especially due to the strongly varying Prandtl numbers in geo- and astrophysical flows.

In the present work, we conduct direct numerical simulations across an extended range of fluids applicable to geo- and astrophysical convection systems while prescribing constant vertical temperature gradients at the horizontal top and bottom planes. Providing extraordinarily long evolution times for each run, we confirm that supergranule aggregation is an omnipresent feature independently of the working fluid. Despite its involved hierarchy of different large-scale flow structures, the global heat and momentum transport of the flows shares similarities with the complementary turbulent superstructures that manifest in the case of applied constant temperatures. Interestingly, the potentially forming stable stratification in the bulk of the convection layer is no necessity for a supergranule aggregation.

2. Numerical method

We consider the simplest conceivable scenario of convection based on the Oberbeck-Boussinesq approximation (Oberbeck 1879; Boussinesq 1903) where the key idea is that the dependence of material parameters on 'pressure is unimportant and that even the variation with temperature may be disregarded except in so far as it modifies the operation of gravity' (Rayleigh 1916). As a consequence, the mass density ρ becomes a linear function of only the temperature when it acts together with gravity but is constant or incompressible otherwise.

The three-dimensional equations of motion are solved by the spectral-element method Nek5000 (Fischer 1997; Scheel et al. 2013). The equations are made dimensionless based on the layer height H and the applied constant vertical temperature gradient β at the plates, resulting in βH as the characteristic temperature scale. Together with the free-fall inertial balance, the free-fall velocity $U_{\mathrm{f}} = \sqrt{g\alpha\beta H^2}$ and free-fall time scale $\tau_{\mathrm{f}} = 1/\sqrt{\alpha g \beta}$ establish as characteristic units. Here, α is the volumetric thermal expansion coefficient at constant pressure and g the acceleration due to gravity. This translates the equations eventually into

$$\nabla \cdot \boldsymbol{u} = 0, \tag{2.1}$$

$$\frac{\partial \boldsymbol{u}}{\partial t} + (\boldsymbol{u} \cdot \nabla)\, \boldsymbol{u} = -\nabla p + \sqrt{\frac{\mathrm{Pr}}{\mathrm{Ra}}}\, \nabla^2 \boldsymbol{u} + T \boldsymbol{e}_z, \tag{2.2}$$

$$\frac{\partial T}{\partial t} + (\boldsymbol{u} \cdot \nabla)\, T = \frac{1}{\sqrt{\mathrm{RaPr}}}\, \nabla^2 T \tag{2.3}$$

with $\boldsymbol{u}$, T, and p representing the velocity, temperature, and pressure field, respectively. The relative strength of the individual terms in these equations is controlled by the Rayleigh and Prandtl number,

$$\mathrm{Ra} := \frac{\alpha g \beta H^4}{\nu \kappa} \qquad \text{and} \qquad \mathrm{Pr} := \frac{\nu}{\kappa}, \tag{2.4}$$

only. The quantities ν and κ denote the viscous and thermal diffusivity, respectively, and thus define the strength of molecular diffusion processes.

Independently of Ra and Pr, equations (2.1) – (2.3) are complemented by a three-dimensional domain with a square horizontal cross-section $A = \Gamma \times \Gamma$ and an aspect ratio $\Gamma := L/H = 60$ where L is the horizontal periodic length of the domain. We apply at the top and bottom planes mechanical free-slip boundary conditions

$$u_z \ (z \in \{0, 1\}) = 0, \quad \frac{\partial u_{x,y}}{\partial z} \ (z \in \{0, 1\}) = 0, \tag{2.5}$$

as well as thermal constant heat flux boundary conditions

$$\frac{\partial T}{\partial z} \ (z \in \{0, 1\}) = -1. \tag{2.6}$$

In spite of our interest in *large*-scale flow structures, our direct numerical simulations resolve all dynamically relevant scales of the flows ranging from the domain size down to the dissipation scales. The latter are given by the so-called Kolmogorov and Batchelor scale (Kolmogorov 1991; Batchelor 1959; Sreenivasan 2004),

$$\eta_\mathrm{K} := \frac{\mathrm{Pr}^{3/8}}{\mathrm{Ra}^{3/8}\, \varepsilon^{1/4}} \quad \text{and} \quad \eta_\mathrm{B} := \frac{\eta_\mathrm{K}}{\sqrt{\mathrm{Pr}}}, \tag{2.7}$$

for the velocity and scalar temperature field, respectively, where $\varepsilon := (1/2)\sqrt{\mathrm{Pr}/\mathrm{Ra}} \left[(\nabla \boldsymbol{u}) + (\nabla \boldsymbol{u})^T \right]^2$ represents the kinetic energy dissipation rate. Note that while the Batchelor scale $\eta_\mathrm{B} \leqslant \eta_\mathrm{K}$ applies for $\mathrm{Pr} \geqslant 1$, the Corrsin scale $\eta_\mathrm{C} := \eta_\mathrm{K}/\mathrm{Pr}^{3/4}$ (Corrsin 1951) is here not of particular interest as it applies only at $\mathrm{Pr} \leqslant 1$ where $\eta_\mathrm{C} \geqslant \eta_\mathrm{K}$.

3. Results

In contrast to our previous work (Vieweg et al. 2021), we fix here the Rayleigh number $\mathrm{Ra} \approx 2.0 \times 10^5$ but vary instead the Prandtl number $\mathrm{Pr} \in \left[10^{-2}, 10^2\right]$ across 4 orders of magnitude centred around $\mathrm{Pr} = 1$. The precise parameters are summarised for all our simulation runs in table 1.

3.1. *Ubiquitous gradual supergranule aggregation*

Every simulation is run as long as necessary to indicate a stationarity of the large-scale flow structure formation. This can be captured, for instance, by (i) the thermal variance Θ_rms with $\Theta = T - T_\mathrm{lin}$ and the linear conduction profile $T_\mathrm{lin} := 1 - z$ or (ii) the integral length scale (Parodi et al. 2004) of the temperature field

$$\Lambda_T \left(z_0, t\right) := 2\pi \frac{\int_{k_\mathrm{h}} \left[E_{TT} \left(k_\mathrm{h}, z_0, t\right) / k_\mathrm{h}\right] dk_\mathrm{h}}{\int_{k_\mathrm{h}} E_{TT} \left(k_\mathrm{h}, z_0, t\right) dk_\mathrm{h}} \tag{3.1}$$

based on the azimuthally averaged Fourier energy spectrum at midplane, $E_{TT} \left(k_\mathrm{h}, z_0 = 0.5, t\right)$, as shown in (Vieweg et al. 2022). Note here that both the Reynolds and Nusselt number (see below in equations (3.2) and (3.3), respectively) are not suitable to capture the transient

Run	Pr	N_e	N	$t_r\,[\tau_f]$	$t_r\,[\tau_\nu]$	$t_r\,[\tau_\kappa]$	Λ_T	Nu	Re
Nfs2_Pr001	0.01	$830^2 \times 16$	13	5,575	1.2	123.6	59.65 ± 0.00	3.17 ± 0.01	2063.0 ± 0.7
Nfs2_Pr01	0.1	$400^2 \times 8$	9	4,250	3.0	29.8	59.71 ± 0.01	4.94 ± 0.09	433.0 ± 3.4
Nfs2	1	$200^2 \times 4$	11	6,500	14.4	14.4	59.66 ± 0.02	6.74 ± 0.10	81.4 ± 0.7
Nfs2_Pr7	7	$200^2 \times 4$	7	4,000	23.5	3.4	59.76 ± 0.01	7.21 ± 0.14	16.2 ± 0.2
Nfs2_Pr10	10	$200^2 \times 4$	7	6,000	42.1	4.2	59.80 ± 0.01	7.13 ± 0.10	11.7 ± 0.0
Nfs2_Pr100	100	$200^2 \times 4$	7	14,000	310.3	3.1	59.78 ± 0.02	7.02 ± 0.03	1.1 ± 0.0

Table 1: Simulation parameters of the direct numerical simulations at different Prandtl numbers Pr – the Rayleigh number Ra = 203,576, aspect ratio $\Gamma = 60$, and free-slip as well as constant heat flux boundary conditions are applied for all runs. The table contains further the total number of spectral elements N_e in the simulation domain, the polynomial order N on each spectral element, the total runtime of the simulation t_r in units of the corresponding free-fall times τ_f, a subsequent translation of these runtimes into diffusion times $\tau_{\nu,\kappa}$, as well as the integral length scale Λ_T of the temperature field at midplane, the resulting Nusselt number Nu, and the Reynolds number Re. Nu and Re are determined from several thousand iterations, whereas Λ_T is based on 50 (10 for Nfs2_Pr001) snapshots within the last $5\tau_f$ in case of Nfs2_Pr001, $1000\tau_f$ in case of Nfs2_Pr100, or $500\tau_f$ in case of any other simulation run. Error bars are determined based on the standard deviation.

large-scale structure formation (Vieweg et al. 2021, 2022). Running our simulations reveals two particularly interesting results.

Firstly, the gradual supergranule aggregation – first reported in (Vieweg et al. 2021) – sets in even beyond Pr = 1 at all accessible Prandtl numbers as both Θ_{rms} and Λ_T increase over time, see also figure 2. Yet, the varying diffusivities affect the pace of the dynamics and thus the necessary simulation runtime t_r to reach a statistically stationary large-scale pattern size, see table 1. Although t_r is by far largest for the upper investigated limit of Pr, we find a similar trend in the opposing lower limit. This observation confirms that the efficiency of the aggregation process depends on the interplay of the velocity and temperature field, being in line with our previous results (Vieweg et al. 2022) which trace the (thermal) supergranule aggregation basically back to an *advective transfer of thermal variance*. Consequently, these runtimes do not support any relation to the diffusive time scales $\tau_\nu = H^2/\nu \equiv \sqrt{\mathrm{Ra/Pr}}\ \tau_f$ and $\tau_\kappa = H^2/\kappa \equiv \sqrt{\mathrm{RaPr}}\ \tau_f$ as contrasted in table 1. Interestingly, while more simulations are required to draw firm conclusions on the interplay of diffusion processes concerning the pace of the aggregation process, the increase of necessary runtime is clearly larger in the direction $\mathrm{Pr} \to \infty$.

Secondly, this process ceases – independently of Pr – only once the horizontal domain size is reached, implying that thermal variance has significantly aggregated on the scale of the horizontal domain size. Consequently, the integral length scale Λ_T converges in any simulation run towards Γ as shown in table 1 and figure 2 (b). Figure 3 visualises the temperature and vertical velocity field in horizontal planes within the upper thermal boundary layer for these final states of the flows. In particular, panels (a, i, k, o, q) depict the temperature fields across the entire horizontal cross-sections of the domains, whereas panels (c, f, m, p, r) exemplary contrast them to the velocity field with respect to its vertical component. The circumstance that the supergranules grow in every run without any upper physical limit confirms that the secondary instability mechanism (Chapman and Proctor 1980; Chapman et al. 1980) rules the formation of long-living large-scale flow structures even far beyond the onset of convection independently of Pr.

Albeit the gradual supergranule aggregation seems to be a ubiquitous feature across all covered fluids, the variation of the Prandtl number still modifies other aspects of the flow.

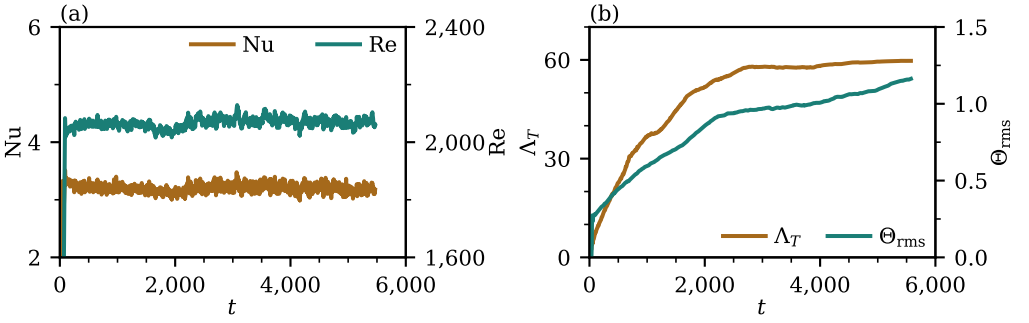

Figure 2: Signs of the transient supergranule aggregation. (a) While neither Nu nor Re are sigificantly affected, (b) Λ_T and $\Theta_{\rm rms}$ do indicate the transient supergranule aggregation. The data corresponds to $\mathrm{Pr} = 10^{-2}$, see also figure 1.

While they display well-ordered stems of localised up- and down-flow regions for large Pr, they become increasingly disordered for increasingly smaller Pr due to the reduced importance of molecular friction. Consequently, the ranges of observable scales or details diverge when comparing the temperature and vertical velocity field – this is highlighted in figure 3 by magnifications of fractions of the flows. In case of $\mathrm{Pr} = 1$, both fields offer an equivalent richness of details which is shown in panels (l, n). This changes once the Prandtl number moves off unity and the diffusivities of momentum and the scalar temperature or the mean Kolmogorov (Kolmogorov 1991) and Batchelor (Batchelor 1959) scales differ. On the one hand, the temperature field becomes successively diffuse or imprecise for increasingly smaller Pr, compare thereto panels (b, j, l). On the other hand, the velocity field becomes simultaneously successively more chaotic as directly contrasted in panels (d, g, n). The tremendous scale separation between the two fields is ultimately highlighted by further magnifications of even smaller regions in panels (e, h), underlining the vast complexity of low-Pr thermal convection flows.

The increasing local disparity of the temperature and velocity field due to the different time scales of the underlying diffusion processes suggests to investigate the impact of a variation of Pr on the global transport of momentum and heat in the following.

3.2. *Global transport properties and the role of stratification*

An alternative perspective on the response of the dynamical system on its buoyancy-induced forcing is its global momentum and heat transport as can be measured by the Reynolds and Nusselt number, respectively. While the former is given by

$$\mathrm{Re}\,(t) := \sqrt{\frac{\mathrm{Ra}}{\mathrm{Pr}}}\,u_{\rm rms} \qquad \text{with } u_{\rm rms} := \sqrt{\langle \boldsymbol{u}^2 \rangle_V}, \tag{3.2}$$

the latter quantifies the strength of convective heat transport across the fluid layer compared to pure heat conduction and results (in the present case of an applied constant heat flux) in (Otero et al. 2002)

$$\mathrm{Nu}\,(t) = \frac{1}{\Delta T_{\rm N}} \qquad \text{with } \Delta T_{\rm N} := \langle T(z=0) - T(z=1) \rangle_A \leqslant 1 \tag{3.3}$$

where $\Delta T_{\rm N}$ is the dynamically manifesting mean temperature drop across the fluid layer.

Figure 4 visualises via dark markers the dependence of these global transport measures on the Prandtl number for the final flow states, see again figure 3. On the one hand, the Reynolds number can be found to increase steadily when the Prandtl number is decreased. This is in

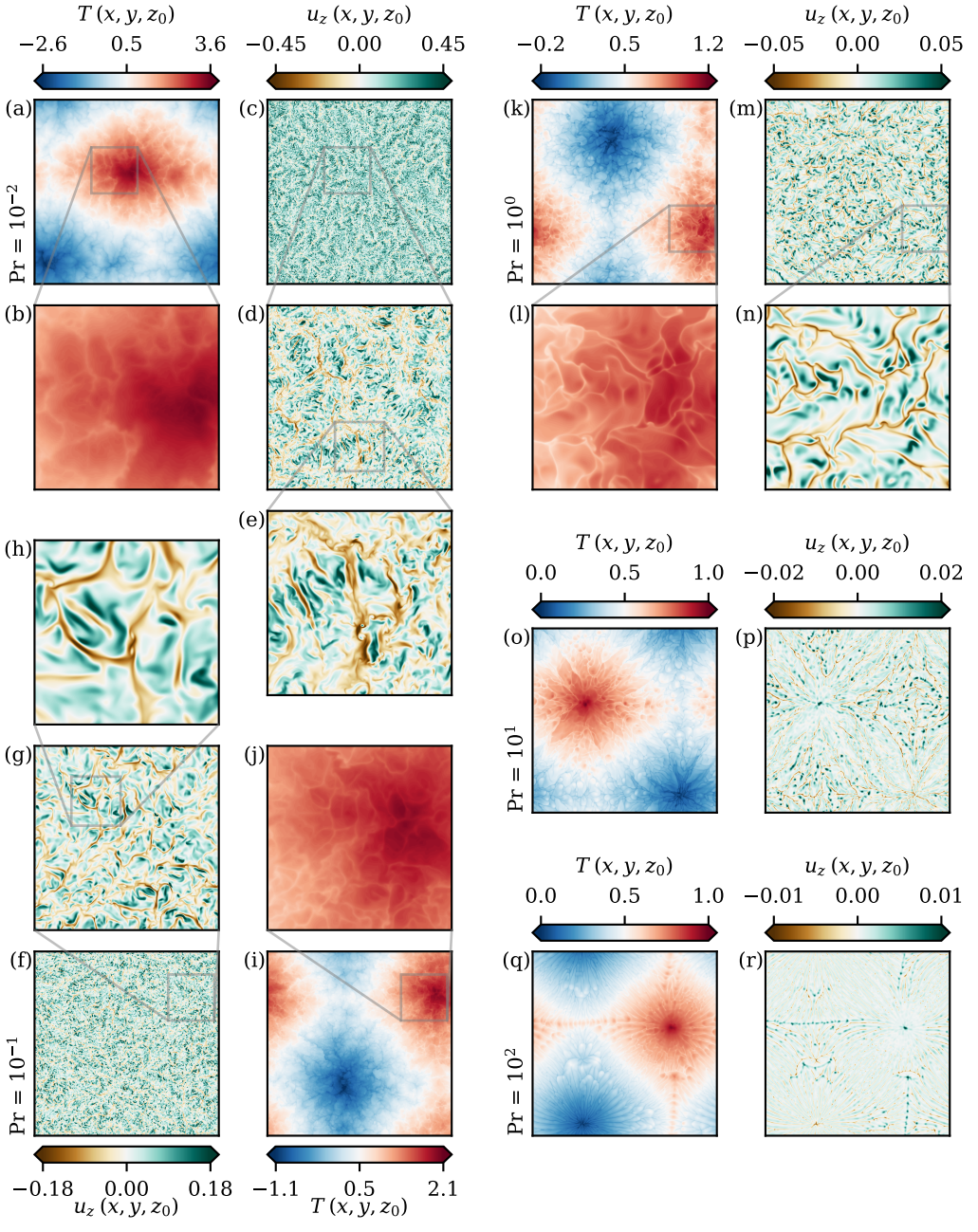

Figure 3: Supergranulation across 4 orders of Prandtl numbers. Although the velocity field exhibits successively smaller features for decreasing Prandtl numbers Pr, the supergranule aggregation can still easily be observed in the temperature field. Panels (a, c, f, i, k, m, o, p, q, r) visualise the entire cross-section at $z_0 = 1 - \delta_T/2$. To highlight the vast scale-separation between the temperature and (vertical) velocity field for small Pr, panels (b, d, g, j, l, m) enlarge a region of interest of size 15×15. Panels (e, h) underline this fact by additional magnifications of regions of size 4×4.

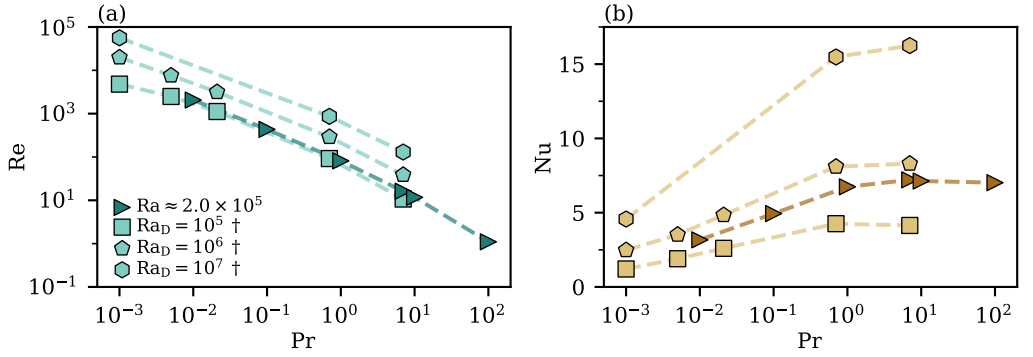

Figure 4: Global convective momentum and heat transport for different fluids. (a) While the global momentum transport increases with decreasing Pr, (b) the convective heat transport loses importance only for $\mathrm{Pr} \lesssim 1$. The *dark* markers correspond to supergranule data from the late state of this study's flows as described by table 1. In contrast, the *bright* markers represent turbulent superstructure data (i.e., different thermal boundary conditions) as outlined in the discussion. In a nutshell, the present study differs from †(Pandey et al. 2022) as follows: thermal Neumann boundary conditions vs. Dirichlet conditions, horizontally periodic domain of $\Gamma = 60$ vs. closed box of $\Gamma = 25$, mechanical free-slip boundary conditions at the top and bottom planes vs. no-slip conditions.

accordance with the vanishing role of viscous diffusion, allowing for higher velocities and leading to successively more inertial flows. As this holds for the entire range of covered Prandtl numbers, it implies that the flow laminarises for $\mathrm{Pr} \gg 1$. On the other hand, the Nusselt number shows a more complex behaviour. For decreasing Prandtl numbers in the range $\mathrm{Pr} \lesssim 1$, thermal diffusion gains relevance as the disorder in the flow intensifies (see Re). In contrast, Nu stagnates for $\mathrm{Pr} \gtrsim 1$ – this effect might be induced by the full nesting of the thermal boundary layer into the viscous one (Chilla and Schumacher 2012) (the latter of which might be estimated to be $\delta_u \sim \mathrm{Pr}\ \delta_T$ based on diffusion arguments), so buoyancy effects get suppressed or protracted by viscous diffusion and thermal plumes detach less frequently.

Thermal plume detachments are fundamentally driven by the applied (inverse or) *unstable density stratification* introduced at the heated bottom and cooled top plane. These ascending and descending plumes leave consequently the boundary layers and travel – driven by buoyancy – into or even through the bulk, leading to turbulent mixing once the flow is sufficiently inertial. Remarkably, our previous study (Vieweg et al. 2021) observed a slightly *stable density stratification* for any constant heat flux-driven convection flow in the bulk region independently of Ra given $\mathrm{Pr} = 1$. In other words, the flow structures established a density stratification that was counter-directed to the applied one. Although the strength of this stratification decreased with increasing Ra, it remained stable for all accessible $\mathrm{Ra} \lesssim 10^8$. In the following, we address the question if such a stable stratification is a unique feature of every flow that exhibits the effect of supergranule aggregation.

Therefore, we contrast the temperature profiles of all present runs in figure 5 (a). Note that the temperature fields are re-scaled here via $T_{\mathrm{rs}} = (T - \langle T \rangle_V) / \Delta T_{\mathrm{N}} + \langle T \rangle_V$ (which does not affect the stratification properties) to allow for a direct comparison. Unlike in our previous study, we find here stably as well as unstably stratified bulks despite the presence of supergranules for any Pr. While it is stable for $\mathrm{Pr} \geqslant 1$ and converges for $\mathrm{Pr} \gtrsim 7$, it is increasingly unstable for successively smaller Prandtl numbers $\mathrm{Pr} < 1$. Interestingly, these trends coincide with the above findings regarding the scaling of Nu (Pr), suggesting a relation of the bulk stratification with plume detachments. Hence, a stable stratification in the bulk is no omnipresent result of the emergence of supergranular flow structures.

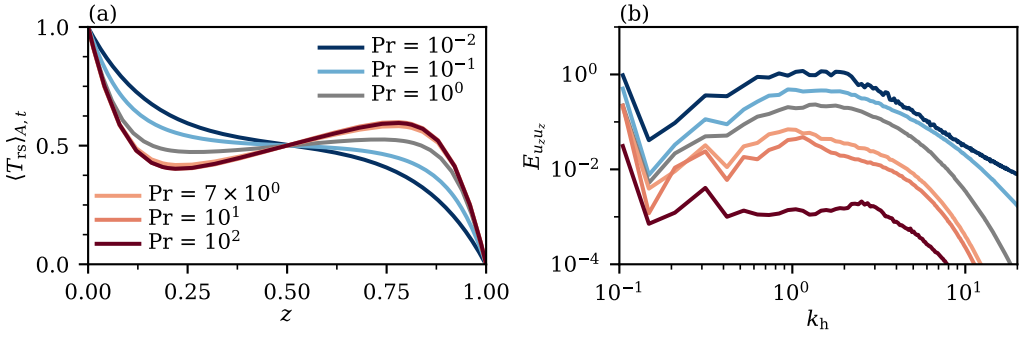

Figure 5: Stratification and the dominance of supergranular flow structures in different fluids. (a) A stable stratification in the bulk – as reported in (Vieweg et al. 2021) – is no necessity for or omnipresent result of the emergence of the supergranule but rather related to plume detachments. The temperature fields are re-scaled as described in the text, and the data correspond to the late state of the flows. (b) Simultaneously, the supergranules at $k_{\mathrm{h,\,min}} = 2\pi/\Gamma \approx 0.1$ become weaker relative to smaller-scale structures for decreasing Pr.

4. Discussion and perspective

The present study raises the question if mechanisms similar to the secondary instability in constant heat flux-driven Rayleigh-Bénard convection (Chapman et al. 1980; Chapman and Proctor 1980) act beyond Pr = 1 (Vieweg et al. 2021) independently of the working fluid and in particular even down to very small Prandtl numbers as found in the solar convection zone (Schumacher and Sreenivasan 2020; Rincon and Rieutord 2018). We therefore conducted a series of simulations across 4 orders of Pr given a fixed thermal driving in a horizontally extremely extended periodic domain of $\Gamma = 60$. We confirmed the presence of the gradual supergranule aggregation as a particular mechanism of self-organisation of long-living large-scale flow structures in naturally forced convection flows independently of the working fluid. Our observations thus suggest that these secondary instabilities dominate any basic heat flux-driven convection flow, leading to a robust hierarchy of different large-scale flow structures.

This omnipresent appearance is in accordance with the accessibility of large-scale $k_z = 0$ spectral modes in the temperature field for this particular thermal boundary condition compared to the classical case of applied constant temperatures (Vieweg et al. 2022). As the present configuration corresponds to a ratio of thermal diffusivities $\kappa_{\mathrm{f}}/\kappa_{\mathrm{s}} \to \infty$, this mechanism can be seen as the result of a relaxation of thermal perturbations that happens much quicker in the fluid compared to in the solid plates (Hurle et al. 1967; Käufer et al. 2023). Moreover, the strength of buoyancy effects is in the heat flux-driven scenario not limited by prescribed temperatures at the boundaries but instead via only the less restrictive mixing of fluid in between. Hence, these arguments allow and demand eventually the formation of horizontally extended flow structures that might even span across the entire domain to advectively transfer the thermal variance.

Given the fact that the variation of the working fluid affects the relative strength of thermal diffusion as described by equation (2.4), one might expect a *de*crease of thermal variance for decreasing Pr due to an increase of κ. However, it turns out that the thermal variance *in*creases – this is also indicated by the colour scales in figure 3. This observation can be explained as follows: smaller Pr result in larger Re and thus in an increased *local* mixing (with κ acting also locally). As the flow is increasingly disordered, the large-scale supergranule becomes less dominant compared to smaller-scale velocity structures which is confirmed by the spectral analysis captured in figure 5 (b). Consequently, the horizontal mixing on large scales (see also the paragraph above) becomes successively less effective for smaller Pr. Note

here that the vanishing stable stratification is not an effect of the increased Reynolds number (Vieweg et al. 2021).

Interestingly, despite the fundamentally different long-living large-scale flow structures between the cases of applied constant temperatures and vertical temperature gradients, their response on a variation of the working fluid shares clear analogies – compare therefore the dark and bright markers in figure 4, respectively. Note here that while the Rayleigh number $\mathrm{Ra_D} := \alpha g \Delta T H^3/(\nu\kappa)$ in case of an applied constant temperature difference ΔT, this is related via $\mathrm{Ra_D} \equiv \mathrm{Ra/Nu}$ (Otero et al. 2002; Vieweg et al. 2021; Foroozani et al. 2021) to equation (2.4). In particular, this allows to relate the present $\mathrm{Pr} = 1$ run to the corresponding no-slip and $\mathrm{Ra_D} = 10^5$ one from (Pandey et al. 2022) as described in (Vieweg et al. 2021). Thus, the particular kind of thermal boundary condition seems not to be of great significance when it comes to qualitative trends of the classical global measures of heat and momentum transport with respect to Pr. Moreover, this underlines that diffusion processes are primarily *locally* important and do not rule the large-scale pattern formation.

The omnipresence of supergranule aggregation across all accessible Rayleigh and Prandtl numbers highlights the importance of an understanding of secondary (and subsequent) instabilities (Chapman et al. 1980; Chapman and Proctor 1980) slightly above the onset of convection. It is intriguing that such mechanisms survive even into the fully turbulent states of the flows (Vieweg et al. 2021) where patterns are typically highly susceptible to the influence of instabilities and defects on each other (Busse 1978, 2003). Moreover, additional physical mechanisms are required to stop the gradual supergranule aggregation before reaching the numerically finite domain size. Weak rotation around the vertical axis has turned out to effectively interrupt this process in the turbulent regime (Vieweg et al. 2022) while also the primary instability changes qualitatively with $k_{\mathrm{h,\,crit}} > 0$ once rotation is only strong enough (Dowling 1988; Takehiro et al. 2002). Interestingly, the ratio of thermal diffusivities $\kappa_\mathrm{f}/\kappa_\mathrm{s}$ promises similar effects (Hurle et al. 1967). This is of particular importance to better resemble the motivating geo- and astrophysical flows and will be addressed in future studies.

Acknowledgements. The author thanks Prof. J. Schumacher for valuable comments on the early manuscript.

Funding. The author is supported by the Deutsche Forschungsgemeinschaft within the Priority Programme DFG-SPP 1881 'Turbulent Superstructures' as well as grant no. 1410/31-1. He gratefully acknowledges the Gauss Centre for Supercomuting e.V. (www.gauss-centre.eu) for funding this work by providing computing resources on the GCS supercomputer SuperMUC-NG at Leibnitz Supercomputing Centre within project pn68ni and through the John von Neumann Institute for Computing (NIC) on the GCS supercomputer JUWELS at Jülich Supercomputing Center (JSC) within projects mesoc and nonbou. Additionally, he acknowledges the computing centre of the Technische Universität Ilmenau for providing access to, as well as computing and storage resources on its compute cluster MaPaCC4.

Declaration of interests. The author reports no conflict of interest.

Author ORCIDs. P. P. Vieweg, https://orcid.org/0000-0001-7628-9902

REFERENCES

Atkinson, B. W. and Wu Zhang, J. 1996 Mesoscale Shallow Convection in the Atmosphere, *Rev. Geophys.* **34**, 403–431.

Batchelor, G. K. 1959 Small-Scale Variation of Convected Quantities like Temperature in Turbulent Fluid Part 1. General Discussion and the Case of Small Conductivity, *J. Fluid Mech.* **5**, 113.

Boussinesq, J. V. 1903 *Théorie Analytique de La Chaleur*, Vol. 2 (Gauthier-Villars, Paris, France).

Busse, F. H. 1978 Non-Linear Properties of Thermal Convection, *Rep. Prog. Phys.* **41**, 1929–1967.

Busse, F. H. 2003 The Sequence-of-Bifurcations Approach towards Understanding Turbulent Fluid Flow *Surv. Geophys.* **24**, 269–288.

Chapman, C. J. and Proctor, M. R. E. 1980 Nonlinear Rayleigh–Bénard Convection between Poorly Conducting Boundaries, *J. Fluid Mech.* **101**, 759–782.

Chapman, C. J., Childress, S. and Proctor, M. R. E. 1980 Long Wavelength Thermal Convection between Non-Conducting Boundaries, *Earth Planet. Sc. Lett.* **51**, 362–369.

Chillà, F. and Schumacher, J. 2012 New Perspectives in Turbulent Rayleigh-Bénard Convection, *Eur. Phys. J. E* **35**, 58.

Christensen, U. 1995 Effects of Phase Transitions on Mantle Convection, *Annu. Rev. Earth Planet. Sci.* **23**, 65–87.

Corrsin, S. 1951 On the Spectrum of Isotropic Temperature Fluctuations in an Isotropic Turbulence, *J. Appl. Phys.* **22**, 469–473.

Dowling, T. E. 1988 *Rotating Rayleigh-Bénard Convection with Fixed Flux Boundaries* in *1988 Summer Study Program in Geophysical Fluid Dynamics: The Influence of Convection on Large-Scale Circulations* (Woods Hole Oceanographic Institution, Massachusetts), 230–247.

Fischer, P. F. 1997 An Overlapping Schwarz Method for Spectral Element Solution of the Incompressible Navier–Stokes Equations, *J. Comput. Phys.* **133**, 84–101.

Foroozani, N., Krasnov, D. and Schumacher, J. 2021 Turbulent Convection for Different Thermal Boundary Conditions at the Plates, *J. Fluid Mech.* **907**, A27.

Hanson, C. S., Duvall, T. L., Birch, A. C., Gizon, L. and Sreenivasan, K. R. 2020 Solar East-West Flow Correlations That Persist for Months at Low Latitudes Are Dominated by Active Region Inflows, *A&A* **644**, A103.

Hurle, D. T. J., Jakeman, R. and Pike, E. R. 1967 On the Solution of the Bénard Problem with Boundaries of Finite Conductivity, *Proc. R. Soc. Lond. A* **296**, 469–475.

Käufer, T., Vieweg, P. P., Schumacher, J. and Cierpka, C. 2023 Thermal Boundary Condition Studies in Large Aspect Ratio Rayleigh–Bénard Convection, *Eur. J. Mech. B-Fluids* **101**, 283–293.

Kolmogorov, A. N. 1991 The Local Structure of Turbulence in Incompressible Viscous Fluid for Very Large Reynolds Numbers, *Proc. Math. Phys. Sci.* **434**, 9–13.

Krug, D., Lohse, D. and Stevens, R. J. A. M. 2020 Coherence of Temperature and Velocity Superstructures in Turbulent Rayleigh–Bénard Flow, *J. Fluid Mech.* **887**, A2.

Mapes, B. E. and Houze, R. A. 1993 Cloud Clusters and Superclusters over the Oceanic Warm Pool, *Mon. Wea. Rev.* **121**, 1398–1416.

Maxworthy, T. and Narimousa, S. 1994 Unsteady, Turbulent Convection into a Homogeneous, Rotating Fluid, with Oceanographic Applications, *J. Phys. Oceanogr.* **24**, 865–887.

Oberbeck, A. 1879 Ueber die Wärmeleitung der Flüssigkeiten bei Berücksichtigung der Strömungen infolge von Temperaturdifferenzen, *Ann. Phys. Chem.* **243**, 271–292.

Otero, J., Wittenberg, R. W., Worthing, R. A., Doering, C. R. 2002 Bounds on Rayleigh–Bénard Convection with an Imposed Heat Flux, *J. Fluid Mech.* **473**, 191–199.

Pandey, A., Scheel, J. D. and Schumacher, J. 2018 Turbulent Superstructures in Rayleigh-Bénard Convection, *Nat. Commun. 9*, 2118.

Pandey, A., Krasnov, D., Sreenivasan, K. R. and Schumacher, J. 2022 Convective Mesoscale Turbulence at Very Low Prandtl Numbers, *J. Fluid Mech.* **948**, A23.

Parodi, A., von Hardenberg, J., Passoni, G., Provenzale, A. and Spiegel, E. A. 2004 Clustering of Plumes in Turbulent Convection, *Phys. Rev. Lett.* **92**, 194503.

Pellew, A. and Southwell, R. V. 1940 On Maintained Convective Motion in a Fluid Heated from Below, *Proc. R. Soc. Lond. A* **176**, 312–343.

Rayleigh, L. 1916 On Convection Currents in a Horizontal Layer of Fluid, When the Higher Temperature Is on the under Side, *The London, Edinburgh, and Dublin Philosophical Magazine and Journal of Science* **32**, 529–546.

Rincon, F. and Rieutord, M. 2018 The Sun's Supergranulation, *Living Rev. Sol. Phys.* **15**, 6.

Scheel, J. D., Emran, M. S. and Schumacher, J. 2013 Resolving the Fine-Scale Structure in Turbulent Rayleigh–Bénard Convection, *New J. Phys.* **15**, 113063.

Schneide, C., Vieweg, P. P., Schumacher, J. and Padberg-Gehle, K. 2022 Evolutionary Clustering of Lagrangian Trajectories in Turbulent Rayleigh–Bénard Convection Flows, *Chaos* **32**, 013123.

Schumacher, J. and Sreenivasan, K. R. 2020 Colloquium: Unusual Dynamics of Convection in the Sun, *Rev. Mod. Phys.* **92**, 041001.

Sreenivasan, K. R. 2004 Possible Effects of Small-Scale Intermittency in Turbulent Reacting Flows, *Flow Turbul. Combust.* **72**, 115–131.

Stevens, R. J. A. M., Blass, A., Zhu, X., Verzicco, R. and Lohse, D. 2018 Turbulent Thermal Superstructures in Rayleigh-Bénard Convection, *Phys. Rev. Fluids* **3**, 041501.

Takehiro, S.-I., Ishiwatari, M., Nakajima, K. and Hayashi, Y.-Y. 2002 Linear Stability of Thermal

Convection in Rotating Systems with Fixed Heat Flux Boundaries, *Geophys. Astro. Fluid* **96**, 439–459.

Vieweg, P. P., Scheel, J. D. and Schumacher, J. 2021 Supergranule Aggregation for Constant Heat Flux-Driven Turbulent Convection, *Phys. Rev. Research* **3**, 013231.

Vieweg, P. P., Schneide, C., Padberg-Gehle, K. and Schumacher, J. 2021*a* Lagrangian Heat Transport in Turbulent Three-Dimensional Convection, *Phys. Rev. Fluids* **6**, L041501.

Vieweg, P. P., Scheel, J. D., Stepanov, R. and Schumacher, J. 2022 Inverse Cascades of Kinetic Energy and Thermal Variance in Three-Dimensional Horizontally Extended Turbulent Convection, *Phys. Rev. Research* **4**, 043098.

Vieweg, P. P., Klünker, A., Schumacher, J. and Padberg-Gehle, K. 2024 Lagrangian Studies of Coherent Sets and Heat Transport in Constant Heat Flux-Driven Turbulent Rayleigh–Bénard Convection, *Eur. J. Mech. B-Fluids* **103**, 69–85.